Dilatational rheology of water-in-diesel fuel interfaces: Effect of surfactant concentration and bulk-to-interface exchange

SCHOLARONE™
Manuscripts

Dilatational rheology of water-in-diesel fuel interfaces: effect of surfactant concentration and bulk-to-interface exchange

Shweta Narayan[1], Sourav Barman[2], Davis B. Moravec[3], Brad G. Hauser[3], Andrew J. Dallas[3], Joseph A. Zasadzinski[2] and Cari S. Dutcher[1,2,]*

[1]*Department of Mechanical Engineering, University of Minnesota – Twin Cities, Minneapolis, MN*

[2]*Department of Chemical Engineering and Materials Science, University of Minnesota – Twin Cities, Minneapolis, MN*

[3]*Donaldson Company, Bloomington, MN*

[*]*Corresponding author email: cdutcher@umn.edu*

Abstract

Micrometer-sized water droplets dispersed in diesel fuel are stabilized by the fuel's surface-active additives, such as mono-olein and poly(isobutylene) succinimide (PIBSI), making the droplets challenging for coalescing filters to separate. Dynamic material properties found from interfacial rheology are known to influence the behavior of microscale droplets in coalescing filters. In this work, we study the interfacial dilatational properties of water-in-fuel interfaces laden with mono-olein and PIBSI, with a fuel phase of clay-treated ultra-low sulphur diesel (CT ULSD). First, the dynamic interfacial tension (IFT) is measured using pendant drop tensiometry, and a curvature-dependent form of the Ward and Tordai diffusion equation is applied for extracting the diffusivity of the surfactants. Additionally, Langmuir kinetics are applied to the dynamic IFT results to obtain the maximum surface concentration (Γ_∞) and ratio of adsorption to desorption rate constants (κ). We then use a capillary pressure microtensiometer to measure the interfacial dilatational modulus, and further extract the characteristic frequency of surfactant exchange (ω_0) by fitting a model assuming diffusive exchange between the interface and bulk. In this measurement, $50 - 100$ µm diameter water droplets are pinned at the tip of a glass capillary in contact with the surfactant-containing fuel phase, and small amplitude capillary pressure oscillations over a range of frequencies from $0.45 - 20$ rad/s are applied to the interface, inducing changes in interfacial tension and area to yield the dilatational modulus, $E^*(\omega)$. Over the range of concentrations studied, the dilatational modulus of CT ULSD with either mono-olein or PIBSI increases with a decrease in bulk concentration and plateaus at the lowest concentrations of mono-olein. Characteristic frequency (ω_0) values extracted from the fit are compared with those calculated using equilibrium surfactant parameters (κ and Γ_∞) derived from pendant drop tensiometry, and good agreement is found between these values. Importantly, the

results imply that diffusive exchange models based on the equilibrium relationships between surfactant concentration and interfacial tension can be used to infer the dynamic dilatational behavior of complex surfactant systems, such as the water-in-diesel fuel interfaces in this study.

Introduction

Surfactant-stabilized emulsions, commonly occurring in food[1], pharmaceutics[2] and oil production[3], pose complex and interesting scientific challenges to engineers designing fluid handling systems. For example, water can become entrained in diesel fuel during various stages of transportation, storage and handling, and may be even be condensed within the fuel tank. While passing through a lift pump or other components in the fuel supply line, the entrained water is mechanically emulsified into micrometer-sized droplets, which, if they remain in the fuel, can cause corrosion, fouling and pitting damage to various components of the system.[4] Diesel fuel injection systems are sensitive to this water content in the diesel fuel, and standards mandate a maximum allowable water content of 200 ppmbv in diesel fuels, leading to a requirement of highly efficient coalescing filters or separators to remove water from diesel fuel.[5–7] A critical challenge for water droplet coalescence and separation from fuel arises from the presence of various additives in diesel fuel, which act as interface-stabilizing surfactant molecules.[4] When a fresh interface of water is formed in a bulk phase of diesel fuel, the surfactants adsorb to the newly formed interfacial sites, setting up a concentration gradient between the subsurface and the bulk. The gradient drives diffusive exchange between the interface and the bulk, until the interfacial and bulk surfactant concentrations are in equilibrium. The impact of this surfactant diffusion and adsorption can be observed through time-dependent changes in interfacial tension (IFT) until an equilibrium IFT value is reached. Examples of additives in diesel fuel include mono-olein, an analogue of which naturally occurs in biodiesel,[5,8] and polyisobutylene succinimide (PIBSI), a common deposit control additive,[9–11] pour point depressants, and cold flow improvers. [12,13] Of these, mono-olein is most often used in standard fuel-water separation testing to determine the efficacy of fuel filtration systems.[5]

Both the SAE J1488[14] and ISO 16332[15] test standards[16] for emulsified water separation from diesel fuel include measurements of the IFT between diesel fuel and water, which is used as a metric of performance for how "easy" it is to separate water from a particular diesel fuel. The higher the IFT, the easier it is to separate water and fuel. For SAE J1488, the fuel is initially stripped of polar additives by clay treatment,[17] following which controlled amounts of mono-olein are added and the interfacial tension at a specified time is measured using standard methods such as Du Noüy ring or pendant drop tensiometry.[14] Certain test protocols within ISO 16332 allow for fuels to be used directly from a fuel supplier, and these fuels often contain PIBSI.[14,15] In our recent work, the IFT of water droplets with diesel fuel in the presence of mono-olein and PIBSI was measured on the micrometer length scale using a microfluidic droplet deformation device.[4] This work led to the important conclusion that interfacial tension reaches equilibrium orders of magnitude faster with micrometer-sized droplets (similar to those found in fuel emulsions), particularly in the presence of strong bulk convection, than with millimeter-sized drops typically used to measure interface properties for fuel-water separation testing. Another recent work by our group highlights the importance of interfacial curvature and surfactant-containing phase on time dependent interfacial tension in microscale droplets, while also discussing adsorption isotherms and models used to extract surfactant properties from dynamic IFT data.[18]

Beyond dynamic IFT, which can be used to infer the surfactant diffusive and adsorptive timescales to the interface, the interfacial rheology is also important in understanding the emulsion stability. When droplets are driven together due to flow in a coalescing filter, depending on the flow strength and fluid and interfacial properties, the droplet surfaces may flatten locally around the region of apparent contact, leading to the formation of a thin fuel film

between the droplets.[19] As the thin film drains, the interface deforms in both shape and size, resulting in both shear and dilatational interfacial kinematics. This interfacial deformation leads to surfactant motion at and along the interfaces, which impacts the rheological response to the deformation. Interfacial shear rheology garnered more attention and has historically been studied using bicone[20] or knife-edge rheometers,[21] double wall rings[22] mounted on rotational rheometers, oscillating needles[23–26] and rotating microbuttons[27–32]. In a shear deformation, the interface changes shape at a constant area. For many soluble surfactants such as mono-olein and PIBSI, the interfacial shear modulus is very small[33] and can be assumed to be negligible.[32] On the other hand, the interfacial shear viscosity can be significant for particle- or insoluble surfactant-laden monolayers, and has been shown to correlate with emulsion stability.[34] Of likely equal importance, but much less studied, interfaces of coalescing droplets can be subjected to dilatational deformation during collisions.[35] In a dilatational deformation, the interface changes area at a constant shape. Any arbitrary interfacial deformation is a sum of shear and dilatation. The resistance of a droplet to dilatational deformation may often be more significant than the shear resistance,[33,36,37] especially for the soluble surfactants considered here.[32] The role of surfactant transport to curved interfaces in droplet interactions and coalescence has recently been reviewed in Narayan et al.[35] and Chen et al.'s[18] works.

The dilatational modulus, $E^*(\omega) = A\left(\frac{\partial \gamma}{\partial A}\right)$, relates the change in interfacial tension, γ, to the change in interfacial area, A, at an oscillation frequency, ω. Dilatational rheological properties have been measured in Langmuir troughs with movable barriers, which employ flat interfaces,[38,39] or millimeter to centimeter diameter oscillating bubbles or drops with curved interfaces.[40] However, these methods excite both dilatational and shear deformations, and it can be challenging to separate these two effects in practice.[39,41] Moreover, with trough rheometers,

the interfacial dilatational response can be challenging to distinguish from the underlying bulk

flow response.[24,42] To minimize these undesirable effects, these instruments are restricted to low

frequencies (< 1 Hz). However, deformation of droplet interfaces following impact in a filter

likely occurs at shorter timescales, (i.e. higher frequencies), hence it is desirable to understand

the high frequency behavior of these liquid-liquid systems.[36] Moreover, Alvarez and others

found that the mass transfer of surfactant to interfaces is strongly influenced by interfacial

curvature; smaller drops and bubbles equilibrate and exchange material with the bulk phase more

rapidly than flat surfaces.[43–46]

Eliminating shear deformations relative to dilatational deformations is experimentally

challenging, and requires a homogeneous internal capillary pressure unaffected by gravity; any

heterogenous pressure distribution that causes the bubble or drop to deviate from a spherical

shape leads to shear deformations as the bubble or drop is oscillated.[47] When the Bond number,

$\Delta \varrho g R^2 / \gamma < 0.01,$ bubbles or drops of radius R are small enough that gravity does not alter the

isotropic capillary pressure in the drop, hence the drop takes on a spherical shape of constant

mean curvature.[48] Here, $\Delta \varrho$ is the density difference between the fluids ($\sim$ 200 kg/m³), g is

gravity (9.8 m/s²), and γ is the interfacial tension. In the capillary pressure microtensiometer

(CPM)[46,49,50] (**Figure 1**), $25 - 40$ micrometer radius droplets are held in a glass capillary giving a

Bond number < 0.0003 at the lowest interfacial tension of $\sim$ 10 mN/m for the largest capillary

used, which minimizes the non-dilatational deformation and improves accuracy. To determine

the dilatational modulus, a time varying capillary pressure, $\Delta P(t)$, is imposed between the drop

and the surrounding fluid that induces a change in the hemispherical drop area, *A(t)* (strain) and

the surface or interfacial tension $\gamma(t)$ (stress). To achieve stable pinning of water droplets in the

glass capillaries in this work, a rigorous surface treatment protocol is required, which is detailed

in Section 2. The drop radius and the interfacial tension depend on the pressure oscillation through the Laplace equation, $\gamma(t) = \Delta P(t)R(t)/2$. Hence, the CPM does not impose either a controlled stress or controlled strain rate, but rather the stress and strain rate are coupled via the Laplace equation. In this work, we use the CPM and a perturbation analysis by Kotula and Anna[47] to measure the interfacial dilatational modulus of water-in-diesel fuel systems with mono-olein and PIBSI dissolved in the fuel phase over a frequency range of 0.45 − 20 rad/s. The diesel fuel used in these experiments is clay-treated ULSD, which is a standard base fuel used for fuel-water separation testing in the automotive industry.[5] Pendant drop tensiometry measurements[51] with large, millimeter-sized droplets are also conducted to extract the diffusivities of mono-olein and PIBSI in diesel fuel. These measurements are presented in Section 3.

In Section 4, the characteristic frequency of surfactant exchange with the subphase is determined by fitting a diffusion-limited model developed by Kotula and Anna[47] to the magnitude of the dilatational modulus at low to moderate concentrations of mono-olein and PIBSI. Here, the radius is maintained relatively constant to account for the curvature dependence of the modulus, while the surfactant concentration is varied to examine the correlation between the characteristic frequency of surfactant exchange and the bulk concentration of the surfactant. When the interface is deformed by changing the interfacial area, diffusive transport of the soluble surfactant between the interface and the bulk drives the system towards equilibrium. The frequency at which the interface is deformed determines whether the diffusive transport can keep pace with the interfacial deformation. Based on Lucassen and Van den Tempel's classical model[52] relating the dilatational modulus to diffusive transport between the bulk and interface, Kotula and Anna[47] derived a model accounting for interfacial curvature and viscous resistance of

the interface. Two characteristic frequencies arise from their analysis – one accounts for the curvature of the interface, while the second accounts for surfactant exchange between the bulk and interface. For the complex water-in-diesel fuel interfaces in this study, we show that equilibrium surfactant properties determined by the pendant drop experiments can be used to correlate and predict the dynamics of the dilatational modulus, in particular, the characteristic frequency at which surfactant exchanges with the interface.

Methods and Materials

Capillary pressure microtensiometer
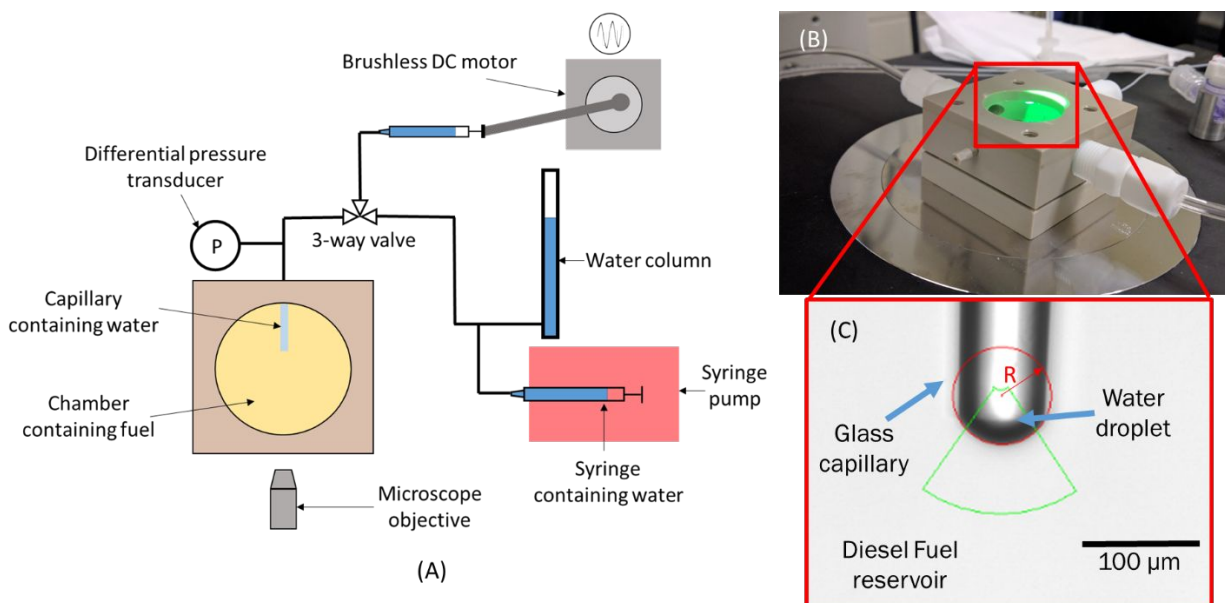
Figure 1: (A) Components of the capillary pressure microtensiometer setup used for dilatational modulus measurements. Proportions are exaggerated for clarity (B) Microtensiometer chamber mounted on the inverted microscope stage (C) Zoomed-in view of the capillary tip inside the microtensiometer chamber. The phase inside the capillary is water, while the surrounding phase is clay-treated ULSD with surfactant.

The capillary pressure microtensiometer (CPM) is based on a previous design by Walker, Anna and coworkers.[43,46,49,53–55] It consists of the following key components as shown in **Figure**

1A: The liquid reservoir is fabricated using PEEK (polyether ether ketone), which is resistant to damage by diesel fuels. Fittings and seals for the chamber, including those for holding the capillary, are made of Teflon (McMaster-Carr). A circular glass viewing window on the bottom of the fluid reservoir (30 mm diameter, Edmund Optics) allows for imaging the capillary and drop shape using an inverted microscope stage (Nikon Eclipse Ti). Images are recorded using a National Instruments Machine Vision camera at 30 frames per second. A differential pressure transducer (Omega Engineering) is used to measure the pressure P_{in} inside the capillary. The outside pressure (P_{out}) is the sum of atmospheric pressure (P_{atm}) and the hydrostatic pressure of the ~ 3 mm column of fuel above the capillary tip (P_h). The capillary pressure is $P_{eq} = P_{in} - (P_{atm} + P_h)$. A water column is connected to the back end of the capillary outside the chamber to apply a hydrostatic pressure head to set P_{eq} in the drop. Oscillations in P_{eq} are imposed by driving a syringe pump (New Era NE-1000) connected to the water column with a brushless DC motor (Omega Motor) with a speed range of $80 - 4000$ rpm to sinusoidally modify the hydrostatic pressure head.[56] The microtensiometer chamber is disassembled and cleaned after every use by sonication in a dilute solution of Simple Green Industrial Cleaner purchased from McMaster-Carr to remove diesel fuel, followed by repeated sonication with organic solvents and water.

Proper surface treatment of the glass capillaries is essential to pin the water droplet at the end of the capillary. The capillaries used for the experiments are fabricated in-house using a commercial pipette puller (Sutter Instruments P-1000). Borosilicate glass capillaries (OD 1.5 mm, ID 1.10 mm) are purchased from Sutter Instruments and pulled to the desired diameter. It is critical to ensure that the end of the micropipette is completely flat, with no ridges or cracks, and with inner radii in the $25 - 40$ μm range. Once fabricated, the capillaries are cleaned and surface-

treated to ensure that the inner surface of the micropipette tip is hydrophilic, while the outer surface is hydrophobic. To achieve this, the micropipettes are cleaned with a 30% H_2SO_4 + Alnochromix (Alconox) solution for 30 min., followed by rinsing with water and ethanol. The back end (larger diameter) of the capillary is attached to a syringe pump (Harvard Apparatus) pushing air through a 10 mL glass syringe (SGE) at a flow rate of 0.4 mL/min, while the front end (smaller diameter) is dipped in a 2% Xiameter silane (Dow Corning) in ethanol solution for three minutes. This step renders the outer surface of the capillary tip hydrophobic. Finally, the pipettes are rinsed with ethanol and baked overnight at 150°C to ensure the outer surface is hydrophobic. The next day, the inner surfaces of the capillaries are washed again with 30% H_2SO_4 + Alnochromix to render them hydrophilic and remove any silane that may have entered the tip during hydrophobic treatment, following which they are filled with deionized water and stored until use. Just prior to use, the water is removed, and a final rinse is performed with ethanol. In addition to the capillaries, the glass viewing window in the chamber is also treated to be hydrophobic to avoid water droplets sticking to the glass surface in the oil reservoir and obscuring the view during the experiment.

Experimental procedure

Interfacial tension measurements were conducted using both pendant drop tensiometry and capillary pressure microtensiometry. Pendant drop measurements were carried out with diesel fuel and dissolved surfactant as the outer phase and water as the drop phase using a Krüss Drop Shape Analyzer (DSA30, Krüss GmbH), following standard protocol.[51] For the CPM, the capillaries are prepared as detailed in Section 2.1. Using a syringe, HPLC grade water is loaded into the capillary such that water fills the tip, after which the diesel fuel - surfactant solution is pipetted into the chamber. A hemispherical cap of water in diesel fuel is formed at the tip of the

capillary by increasing the hydrostatic pressure head via the syringe pump (**Figure 1A**). A custom LabVIEW code[56] is used to detect the edge of the droplet and fit a circle to the hemispherical cap (indicated by the red circle in **Figure 1C**), yielding continuous real-time measurements of the drop radius R. The pressure transducer is used to measure the differential pressure P_{eq}, which is then used to calculate the interfacial tension, γ, using the Laplace equation

$$\gamma = \frac{P_{eq}R}{2} = \frac{(P_{in} - P_{out})R}{2} . \#(1)$$

The droplet interfacial area, A, is:[47]

$$A = 2\pi R\left(R - \sqrt{R^2 - R_c^2}\right)\#(2)$$

in which R_c is the inner radius of the capillary and R is the drop radius (**Figure 1C**).

To determine the frequency dependent dilatational modulus, E^*, capillary pressure oscillations are applied after the interfacial tension has reached equilibrium (less than 1 mN/m change for at least 15 minutes), resulting in a change in droplet area and interfacial tension, while maintaining a hemispherical shape with $\Delta\varrho g R^2 / \gamma < 0.01$. This guarantees that oscillations in the capillary pressure result in a purely dilatational strain on the drop interface except in the immediate vicinity of the capillary tip.[47] Any non-dilatational strains lead to a non-spherical surface.[57] By fitting the drop to a circle, such deviations or slip of the drop in the capillary leads to the data being rejected. Within the image resolution (**Figure 1C**), the droplet is hemispherical up to the pinning line at the capillary tip. While a small fraction of the drop near the capillary tip does likely undergo non-dilatational deformations due to the confinement by the tip, the interfacial shear modulus of many soluble surfactants is effectively zero, so the shear contribution to the total stress is negligible.

The capillary pressure oscillations imposed on the drop induce changes in both the drop area (strain) and the interfacial tension (stress), which are related by the Laplace equation, $\gamma = (P_{eq} + \Delta P)R/2$. The capillary pressure is oscillated by ΔP around the equilibrium capillary pressure, P_{eq}. $\Delta P/P_{eq}$ is limited so the change in drop surface area is less than 10% of the equilibrium area, which, previous work has shown, ensures that the deformation is in the linear viscoelastic regime.[47] Due to the viscoelastic nature of the interface under dilatation, there is a phase lag, ϕ_{RP}, between the pressure and radius oscillation of ΔR around R_{eq}. The phase lag is obtained by applying fast Fourier transforms to the pressure and radius data. From the FFT, the magnitude of the dilatational modulus E^* is calculated based on the perturbation analysis by Kotula and Anna[47] using

$$|E^*| = \frac{b}{1-b}\left(\frac{R_{eq}}{\Delta R}\right)\left(\frac{P_{eq}R_{eq}}{2}\right)\sqrt{\left(\frac{\Delta R}{R_{eq}}\right)^2 + 2\left(\frac{\Delta R}{R_{eq}}\right)\cos\phi_{RP} + 1}, \#(3)$$

where R_{eq}, P_{eq} are the equilibrium or mean radius and capillary pressure across the droplet interface respectively, and b is a geometric factor given by $b = \sqrt{1 - \left(\frac{R_c}{R_{eq}}\right)^2}$. The real ($E'$) and imaginary ($E''$) parts of the modulus are known as the dilatational storage and loss modulus respectively.[33,58] The minimum value of E^* that can be reliably measured is ~ 1 mN/m due to the resolution of measuring ΔP and ΔR. The highest frequency measured is limited to ~ 20 radians/sec due to the camera frame rate used to measure the drop radius.

Materials

The inner or droplet phase in all experiments is HPLC grade water (Fisher Scientific). The outer phase is diesel fuel, specifically ultra-low sulphur diesel (ULSD). ULSD was purchased from Chevron and supplied by Donaldson Company. Polar components and additives

in diesel fuel are removed by treatment with Fuller's earth in accordance with the SAE J1488 standard[14] to yield clay-treated ultra-low sulphur diesel (CT ULSD) with a density of 0.847 g/mL, which forms the base fuel for all the experiments in this work. The surfactants added to diesel fuel are mono-olien and polyisobutylene succinimide (PIBSI). Mono-olein (1-oleoyl-rac-glycerol, CAS #111-03-5, ≥99% Purity) was procured from Sigma Aldrich. A stock solution of 1 mg/mL mono-olein in CT ULSD was prepared, and solutions of 0.001 - 0.5 mg/mL were prepared by serial dilutions. A PIBSI additive package was obtained from a commercial supplier. A stock solution of 0.74 mg/mL of PIBSI additive package in CT ULSD is prepared and is designated as a '10X' dose, with 1X being a recommended standard dose. The additive package is approximately 85% PIBSI by weight, providing an approximate PIBSI concentration of 0.63 mg/mL, which is equivalent to a 10X dose. 0.01X, 0.05X, 0.1X, and 0.5X and 1X doses are prepared by serial dilutions. A molecular weight of 356.6 g/mol is used in calculations for mono-olein, while a molecular weight of 1000 g/mol is used for PIBSI.[9] **Table 1** lists the samples and concentrations used in this study.

Base Fuel	Surfactant	Concentration (X Std. dose)	Concentration (mg/mL)	Concentration (M)
CT ULSD	Mono-olein	-	0.001	2.8×10^{-6}
CT ULSD	Mono-olein	-	0.005	1.4×10^{-5}
CT ULSD	Mono-olein	-	0.01	2.8×10^{-5}
CT ULSD	Mono-olein	-	0.05	1.4×10^{-4}
CT ULSD	Mono-olein	-	0.1	2.8×10^{-4}
CT ULSD	Mono-olein	-	0.25	7.0×10^{-4}
CT ULSD	Mono-olein	-	0.5	1.4×10^{-3}
CT ULSD	Mono-olein	-	0.75	2.1×10^{-3}
CT ULSD	Mono-olein	-	1	2.8×10^{-3}
CT ULSD	PIBSI	0.01	6.3×10^{-4}	6.3×10^{-7}
CT ULSD	PIBSI	0.05	3.1×10^{-3}	3.1×10^{-6}
CT ULSD	PIBSI	0.1	6.3×10^{-3}	6.3×10^{-6}
CT ULSD	PIBSI	0.5	0.031	3.1×10^{-5}
CT ULSD	PIBSI	1	0.063	6.3×10^{-5}

Table 1: Fuel and surfactant systems studied in this work.

Results

Drop curvature can have a significant effect on the time scale for surfactant transport; typical drop sizes used in pendant drop tensiometry are $1 - 3$ mm in diameter, compared to the 50 μm diameter drops in the CPM. Jin et al[59] postulated that the characteristic time for surfactant transport to curved droplet interfaces is given by $\tau_D = \frac{h^2}{D_s}$, in which h is the depletion depth over which the surfactant concentration is altered by adsorption to the interface. The depletion depth for a planar interface, h_p is the volume of solution per unit interfacial area at a given bulk surfactant concentration, C_0 (mol/m³), that includes sufficient surfactant molecules to fully saturate the planar interface, Γ_{eq} (mol/m²) or $h_p = \frac{\Gamma_{eq}}{C_0}$ (**Figure 2**). However, the volume/interfacial area surrounding a spherical interface grows much more quickly than that adjacent to a planar interface, and hence has a far greater surfactant concentration available per unit area.[60] Simple geometry[44] relates the spherical depletion depth, h_s, to the planar diffusion depth, h_p, through the radius, R of the spherical interface:

$$\frac{h_s}{h_p} = \left(\frac{R}{h_p}\right)\left[\left(\frac{3h_p}{R} + 1\right)^{\frac{1}{3}} - 1\right]. \#\#(4)$$
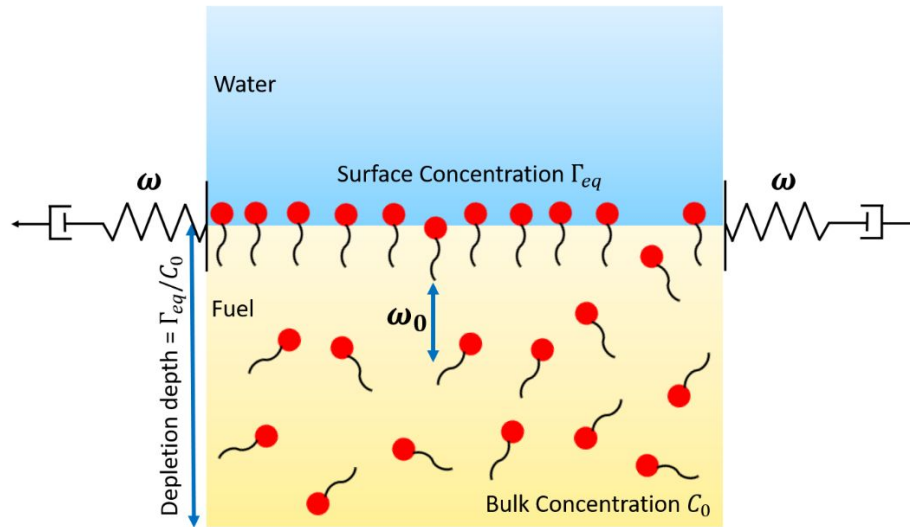
Figure 2 The depletion depth is the volume/area that contains sufficient surfactant concentration, C_0 to fully populate the interface to the equilibrium surface concentration Γ_{eq}. The characteristic frequency for surfactant exchange with the subphase liquid is $\omega_0 = \dfrac{D_s C_0^2}{\Gamma_{eq}^2}$. For $\omega < \omega_0$ surfactant has sufficient time to diffuse on and off the interface, Γ and γ retain their equilibrium values and the dilatational modulus $E^* = A\left(\dfrac{\partial \gamma}{\partial A}\right) \to 0$. For $\omega > \omega_0$ there is insufficient time for surface equilibration with the bulk and E^* is large and measures the surface compressibility similar to an insoluble surfactant.

In the limit that $\dfrac{h_p}{R} \ll 1$, $\dfrac{h_s}{h_p} \to 1$, and there is little effect of drop curvature on surfactant adsorption dynamics. Therefore, in going from a flat interface to a curved interface, not only does one introduce an additional length scale (the radius of the interface, R), but the accompanying decrease in the characteristic time for diffusion may shift the dynamics from being diffusion-controlled to being controlled by the kinetics of adsorption/desorption.[43,45] Therefore, performing interfacial tension measurements with highly curved, micrometer-sized droplets such as the ones used in the CPM, or at extremely high surfactant concentrations, may be a way to access surfactant adsorption/ desorption kinetic parameters.[60] Conversely, using large droplets or planar interfaces allows access to diffusion-limited behavior, particularly if

surfactant concentrations are low. Here, the pendant drop measurements, which are on drops about two orders of magnitude larger than the CPM measurements, serve as a validation of the limiting behavior of CPM measurements and are used to determine approximate values of the diffusivities of mono-olein and PIBSI.

To evaluate $h_p = \Gamma_{eq}/C_0$, we use a Langmuir adsorption model to relate Γ_{eq} to C_0:

$$\Gamma_{eq} = \frac{\Gamma_\infty \kappa C_0}{1 + \kappa C_0} \quad \#(5)$$

in which Γ_∞ is the maximum surface concentration, taken to be the saturation surface concentration at the critical micelle concentration of the particular surfactant, and κ is a measure of relative affinity of a surfactant molecule for the interface, which is equivalent to the ratio of the adsorption to desorption constants in the Langmuir model of adsorption kinetics.[61,62] For this model:

$$h_p = \Gamma_{eq}/C_0 = \frac{\Gamma_\infty \kappa}{1 + \kappa C_0} \quad \#(6)$$

To evaluate the parameters Γ_∞ and κ, we can derive a surface equation of state by integrating the Gibbs adsorption isotherm:[61,62]

$$R_{ig}T\Gamma_{eq} = -C_0\left(\frac{\partial \gamma}{\partial C_0}\right)_T = R_{ig}T\left(\frac{\Gamma_\infty \kappa C_0}{1 + \kappa C_0}\right) \quad \#(7)$$

$\gamma_0 - \gamma = nR_{ig}T\Gamma_\infty ln(1 + \kappa C_0) . \#(8)$ Here, γ_0 is the initial interfacial tension of the clean fuel-water interface, and $n = 1$ for nonionic mono-olein and $n = 2$ for the ionic PIBSI.[61] Fitting Eqn. 8 to the equilibrium interfacial tension vs concentration data for mono-olien and PIBSI in **Figure 3** determines Γ_∞ and κ. Γ_∞ can be independently determined as the slope of the $\gamma_{eq} - lnC$

curve (**Figure 3, inset**) as the CMC concentration is approached:[61] Here, we use the latter approach to minimize the number of fitting parameters and reduce the error in the fit, with Γ_∞ being approximated as

$$\Gamma_\infty \approx -\frac{C_{CMC}}{R_{ig}T}\left(\frac{\partial \gamma}{\partial(C_{CMC})}\right)_T, \#(9)$$
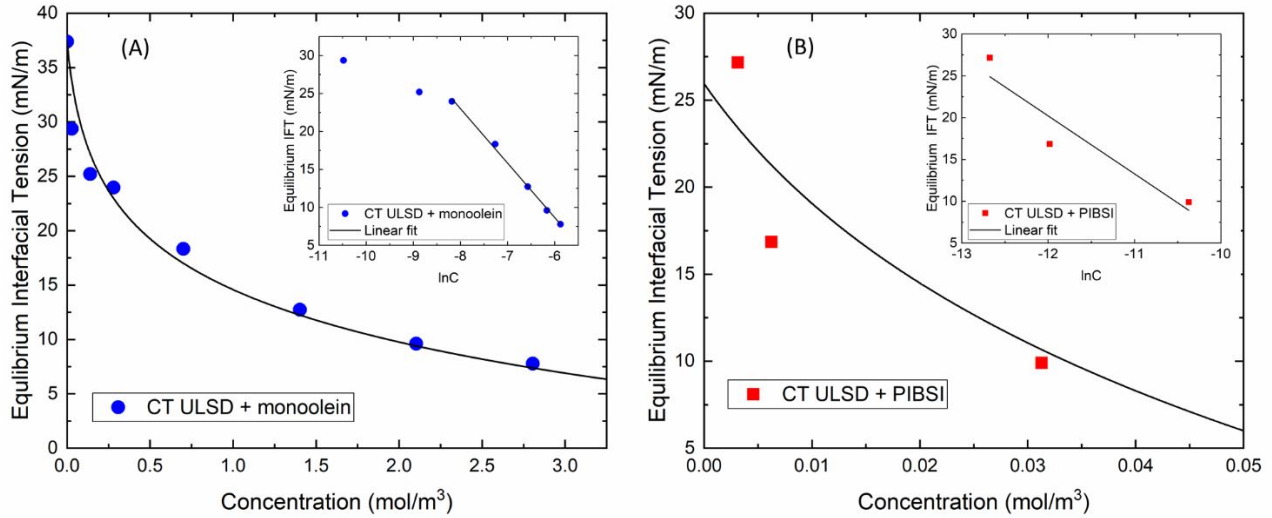
Figure 3 (A) Interfacial tension measurements for CT ULSD systems containing mono-olein using pendant drop tensiometry. Solid black lines are fits of the equation of state (Eqn. 8) to the data with κ as a free parameter. (Inset) Equilibrium interfacial tension as a function of mono-olein concentration in CT ULSD. Solid black line approximates the slope near the CMC concentration of 3 mol/m³ which is related to the maximum surface concentration, $R_{ig}T\Gamma_\infty \approx -\left(\frac{\partial \gamma}{\partial ln(C_{CMC})}\right)_T$ to determine Γ_∞. Data in (A) from Narayan et al., Energy & Fuels (2018) c.f. Figure S7. (B) Interfacial tension measurements for CT ULSD systems containing PIBSI using pendant drop tensiometry. Solid black lines are fits of the equation of state (Eqn. 8) to the data with κ as a free parameter. (Inset) Equilibrium interfacial tension as a function of PIBSI concentration in CT ULSD. Solid black line approximates the slope near the CMC concentration which is related to the maximum surface concentration to determine Γ_∞. (See Table 2).

Best fit values of Γ_∞ and κ are presented in Table 2.   From Eqn. 6, the maximum value of the planar diffusion length as $C_0 \to 0$ is $\Gamma_\infty \kappa$. For $\Gamma_\infty \kappa \ll R$, the interface can be considered planar, while for $\Gamma_\infty \kappa \sim R$, the curvature of the interface will strongly affect the surfactant adsorption. From Table 2, $\Gamma_\infty \kappa = 0.07 \pm 0.01$ mm for mono-olein, and $\Gamma_\infty \kappa = 0.15 \pm 0.14$ mm for PIBSI.

To calculate the diffusivity, the Ward and Tordai model modified for a curved interface of radius R is used to relate the interfacial concentration, $\Gamma_{eq}(t)$, to the bulk concentration, C_0, and C_s, the subsurface concentration immediately adjacent to the interface:[61–63]

$$\Gamma_{eq}(t) = \sqrt{\frac{D_s}{\pi}}\left[2C_0\sqrt{t} - \int_0^t \frac{C_s(\tau)}{(\sqrt{t-\tau})}d\tau\right] + \frac{D_s}{R}\left[C_0 t - \int_0^t C_s(\tau)d\tau\right] \quad (10)$$

D_s is the surfactant monomer diffusivity.[61,64,65] In Eqn. 10, the integral terms describe the back-diffusion of surfactant from the interface to the bulk, while the remaining terms describe adsorption from the bulk. Approximations for the Ward and Tordai equation exist in two limits − 1) The late stages of adsorption in which the interfacial tension is close to equilibrium, i.e. when the subsurface concentration has nearly equilibrated making C_s effectively constant[61,62] and 2) the interfacial tension is close to the value for the pure solvent, i.e. in the early stages of interfacial tension decay, when $C_s \approx 0$ and there is minimal back diffusion of surfactant from the interface.

The interfacial tension of water with CT ULSD without any surfactant is ~44 mN/m,[4] hence it is evident from **Figure 4A** that the rapid early decay of interfacial tension for the mono-olein systems is not captured by pendant drop tensiometry. Therefore, to find the diffusivity of mono-olein, we evaluate Eqn. 10 for a constant C_s, which is valid for long adsorption times:[61–63]

$$\Gamma(t) \cong \sqrt{\frac{D_s}{\pi}} \left[2C_0\sqrt{t} - C_s \int_0^t \frac{d\tau}{(\sqrt{t-\tau})} \right] + \frac{D_s}{R} \left[C_0 t - C_s \int_0^t d\tau \right] = \left[\sqrt{\frac{4D_s t}{\pi}} + \frac{D_s t}{R} \right] (C_0 - C_s) \quad \#\#\#(11)$$

Rearranging gives:

$$(C_0 - C_s) = \frac{\Gamma(t)}{\sqrt{\frac{4D_s t}{\pi}} + \frac{D_s t}{R}} \quad \#(12)$$

Combining this result with the Gibbs adsorption isotherm to evaluate the interfacial tension:

$$\Gamma_{eq} = -\frac{1}{R_{ig}T} \left(\frac{\partial \gamma}{\partial \ln C} \right)_T \quad or \quad -R_{ig}T\Gamma_{eq}d(\ln C) = d\gamma \quad (13)$$

with the approximation that $d(\ln C) \approx \frac{(C_0 - C_s)}{C_0}$ and $d\gamma \approx \gamma_{eq} - \gamma(t)$, combining with Eqn.

11 gives the late-stage solution of the Ward and Tordai model:

$$\gamma(t) - \gamma_{eq} = R_{ig}T\Gamma_{eq} \left(\frac{C_0 - C_s}{C_0} \right) = \frac{\sqrt{\pi}RR_{ig}T\Gamma_{eq}^2}{C_0 \left[R\sqrt{4D_s t} + \sqrt{\pi D_s t} \right]} \quad ,\#(14)$$

In which $\gamma(t)$ is the instantaneous interfacial tension, γ_{eq} is the interfacial tension at equilibrium

$(t \rightarrow \infty)$, R_{ig} is the gas constant, T is the absolute temperature, here 293 K, D_s is the surfactant

diffusivity, t is the time from the initial water-oil contact. The Langmuir model, Eqn. 5 is used

to eliminate $\Gamma_{eq} = \frac{\Gamma_\infty \kappa C_0}{1 + \kappa C_0}$:

$$\gamma(t) - \gamma_{eq} = \frac{\sqrt{\pi}RR_{ig}T \left(\frac{\Gamma_\infty \kappa C_0}{1 + \kappa C_0} \right)^2}{C_0 \left[R\sqrt{4D_s t} + \sqrt{\pi D_s t} \right]} = \frac{\sqrt{\pi}RR_{ig}T(\Gamma_\infty \kappa)^2 C_0}{\left[R\sqrt{4D_s t} + \sqrt{\pi D_s t} \right] (1 + \kappa C_0)^2} \quad (15)$$

The black lines in **Figure 4A** shows the fit of Equation 15 to the mono-olein dynamic interfacial

tension near equilibrium with D_s and γ_{eq} being the only free parameters.
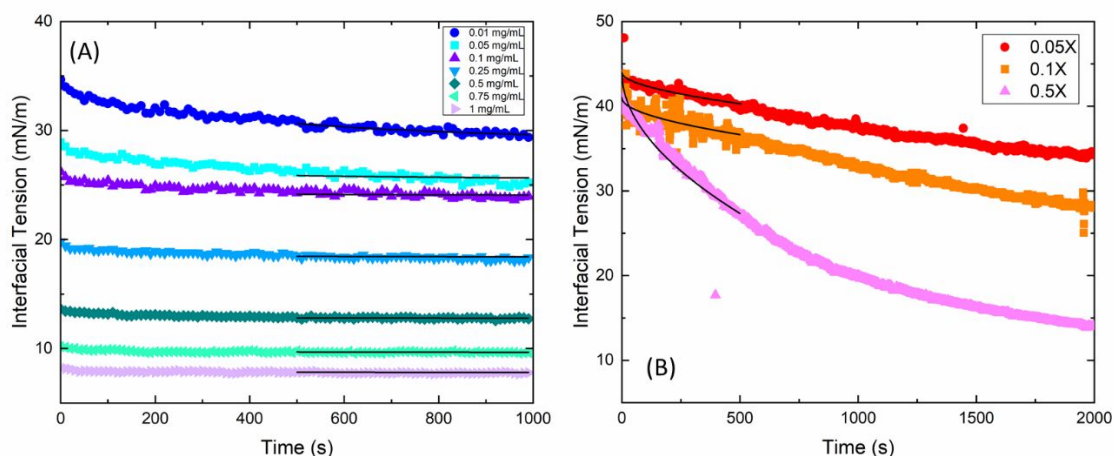
Figure 4 (A) Dynamic Interfacial tension for CT ULSD systems containing mono-olein using pendant drop tensiometry. Solid black lines are fits of Equation (15) to the last 500 seconds of dynamic IFT data. Data in (A) from Narayan et al., Energy & Fuels (2018) c.f. Figure S5.[4] (B) Dynamic Interfacial tension for CT ULSD systems containing PIBSI using pendant drop tensiometry. Solid black lines are fits of Equation (17) to the first 500 seconds of dynamic IFT data.

Figure 4B shows the dynamic oil-water interfacial tension for systems containing the surface-active deposit control additive PIBSI. In general, "PIBSI" is used to indicate a range of chemical structures and molecules, based on a polyisobutylene chain (PIB) with an imide head group,[9] with an average molecular weight of ~1000 g/mol. Unlike mono-olein systems, fuel-water systems containing the cationic surfactant PIBSI have a much slower decrease in interfacial tension with time. It is also important to note that the dynamic interfacial tension of PIBSI does not completely equilibrate even after an hour or more, possibly due to the formation of spontaneous microemulsions along the interface,[66] making it challenging to determine the critical micelle concentration (CMC). At the early stages of surfactant adsorption, there is minimal desorption and back-diffusion of the surfactant from the interface ($C_s \approx 0$ in Eqn 10);

only diffusion from the bulk to the interface is important. The early-stage approximation of the

Ward and Tordai model[61,64] (Eqn. 10) for $C_s \approx 0$ is:

$$\Gamma_{eq}(t) \cong \sqrt{\frac{D_s}{\pi}}[2C_0\sqrt{t}] + \frac{D_s}{R}[C_0 t] = \left[\sqrt{\frac{4D_s t}{\pi}} + \frac{D_s t}{R}\right]C_0 \qquad \#(16a)$$

To connect Γ_{eq} and γ, the Langmuir model can be rearranged and inserted into Eqn 8:

$$\Pi = \gamma_0 - \gamma(t) = -nR_{ig}T\Gamma_\infty\ln\left(1 - \Gamma_{eq}/\Gamma_\infty\right) \#(16b)$$

which, for $\Gamma_{eq}/\Gamma_\infty \ll 1$, reduces to the ideal gas equation of state, $\Pi = nR_{ig}T\Gamma_{eq}$.

$$\Pi = \gamma_0 - \gamma(t) = nR_{ig}T\left[\sqrt{\frac{4D_s t}{\pi}} + \frac{D_s t}{R}\right]C_0.\#(16b)$$

Rearranging gives a relationship between $\Pi = \gamma_0 - \gamma(t)$ and the diffusivity, D_s:

$$\frac{\gamma_0 - \gamma(t)}{nR_{ig}TC_0} = \left[\sqrt{\frac{4D_s t}{\pi}} + \frac{Dt}{R}\right].\#(17)$$

Eqn. 17 is valid only for short times and for small surface pressures near γ_0, and is used to obtain

the surfactant monomer diffusivity D_s for PIBSI. In Eqn. 17, $n = 2$ for an ionic surfactant like

PIBSI. The solid black lines in **Figure 4B** are the fits of Eqn. 17 to the PIBSI dynamic

adsorption data for the first 500 seconds during which surface tension decreases 10- 20%

depending on the PIBSI concentration.

Parameter	Mono-olein	PIBSI
Molecular Weight (g/mol)	356.6	~1000

$\Gamma_\infty \left(\dfrac{\text{mol}}{\text{m}^2}\right)$ (Maximum surface concentration)	$(2.95 \pm 0.09) \times 10^{-6}$	$(2.85 \pm 1) \times 10^{-6}$
κ (m^3/mol) (Ratio of adsorption/desorption rate constants)	23.08 ± 2.73	53.17 ± 34.57
$\kappa\Gamma_\infty$ (mm)	0.07 ± 0.01	0.15 ± 0.14
D_S Surfactant diffusivity (m^2/s)	$(3.28 \pm 1.96) \times 10^{-11}$	$(2.85 \pm 1.14) \times 10^{-11}$

Table 2: Surfactant parameters obtained from pendant drop tensiometry for mono-olein and PIBSI in CT ULSD

Interfacial dilatational modulus using the CPM

In the CPM, capillary pressure oscillations of ΔP around the equilibrium capillary pressure, P_{eq} are determined by a pressure transducer, while the radius change of ΔR around R_{eq} is determined by fitting a circle to a microscope images of the drop. $\Delta P/P_{eq}$ is limited so the change in drop surface area is less than 10% of the equilibrium area.[47] The phase lag between capillary pressure and radius oscillations, ϕ_{RP}, is determined by fast Fourier transforms of the pressure and radius oscillations. The dilatational modulus $|E^*|(\omega) = A\left(\partial\gamma/\partial A\right)$ was calculated from these measured parameters using Eqn. 3 for the range of mono-olein and PIBSI concentrations. The frequency range accessible to the CPM is 0.45 rad/s – 20 rad/s; there are limits on the accuracy of the measurement at higher frequencies. As discussed by Kotula and Anna,[47] Fourier transforms of the pressure and radius oscillations are used to ensure that, for the measurements to be in the linear regime, the magnitude of the applied pressure oscillations is such that ratio of the second harmonic to the first harmonic in the radius is less than 0.1 (10%). Larger harmonic ratios may become prominent at frequencies exceeding 10 rad/s. The minimum pressure and radius oscillations are set by the camera spatial and temporal resolution. Finding the balance between maintaining a small amplitude response and having a deformation large enough

to be detected in the image analysis is the key to performing these experiments successfully. Moreover, unlike air-aqueous systems which have higher surface tensions, the interfacial tensions measured for fuel-water systems can be as low as or even lower than 5 mN/m for PIBSI and mono-olein systems (**Figure 4**).[4] At these low interfacial tensions, the capillary pressure required to form a stable interface is low, and during oscillation startup the droplet may grow uncontrollably, as noted by Kotula and Anna.[47] The maximum capillary pressure is for the minimum drop radius, i.e. when $R_{eq} = R_c$; however, the transient response to interface oscillations can cause the drop to be ejected from the capillary. These factors limit the dilatational modulus measurements for mono-olein to concentrations ≤ 1 mg/ mL and for PIBSI, ≤ 0.5X.[47]
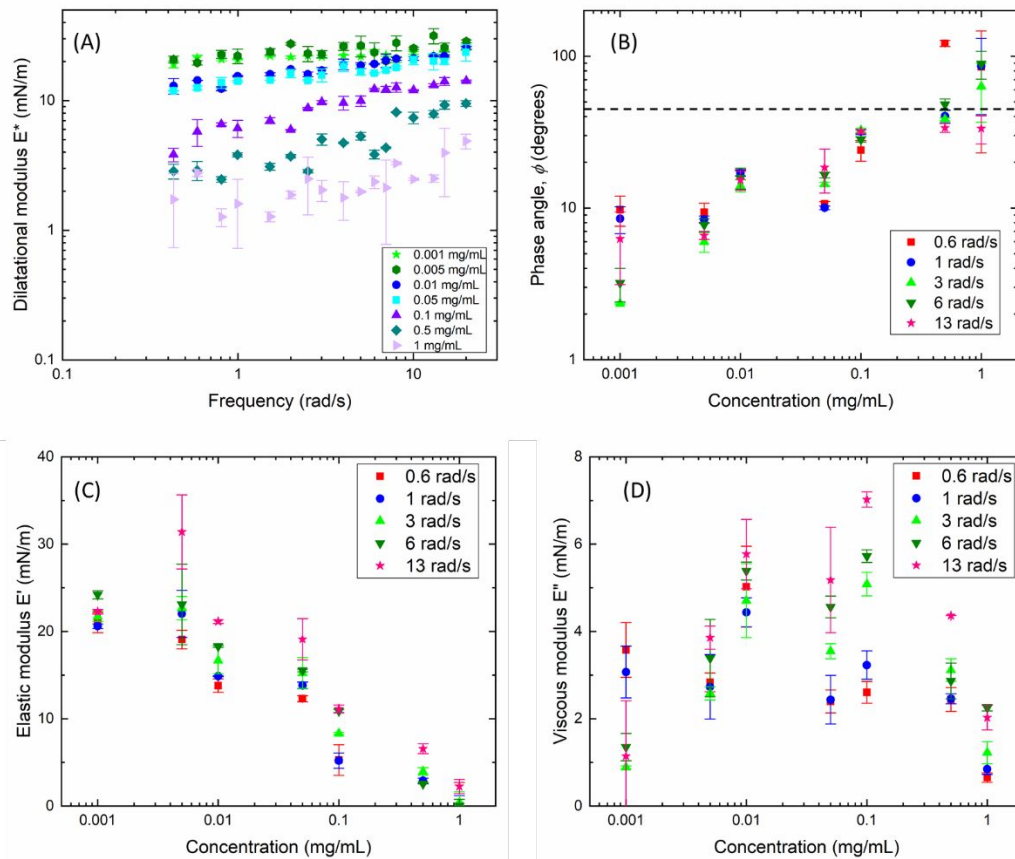
Figure 5 (A) Magnitude of the interfacial dilatational modulus (E*) for mono-olein in CT ULSD as a function of frequency, for various concentrations of mono-olein. (B) Phase angle (ϕ) as a function of mono-olein concentration at selected oscillation frequencies. The phase angle increases with concentration, indicating that the interface transitions gradually from being predominantly elastic at low concentrations to more viscoelastic at high concentrations. The dotted line indicates 45° phase angle. (C) Elastic (storage) modulus (E') as a function of mono-olein concentration at selected oscillation frequencies. E* ~ E' over much of the frequency range. (D) Viscous or loss modulus (E") as a function of mono-olein concentration at selected oscillation frequencies. Note the difference in scale between B, C.

Figure 5A shows the magnitude of E^* as a function of oscillation frequency for water-in-fuel systems stabilized by mono-olein. E^* increases modestly as the frequency increases from $0.45 - 20$ rad/s for all concentrations. This is because, as shown in **Figure 2**, E^* is set by exchange between the interface and subphase by diffusion with a characteristic frequency, ω. If the applied frequency, ω, is less than the characteristic frequency, ω_0, the surface concentration of mono-olein, Γ, remains roughly constant, which in turn, keeps γ constant, and $E^* = A\left(\partial\gamma/\partial A\right)\to 0$ (See Eqn. 6). However, if $\omega > \omega_0$, mono-olein does not have sufficient time to diffuse off the interface, Γ increases and γ decreases as the surface area decreases, and E^* reflects the compressibility of the interface, similar to an insoluble surfactant.[47,56,67] E^* does not appear to plateau at the highest frequencies we can measure, but continues to show an upward trend, especially at the higher surfactant concentrations.[56] What is more clear is that E^* has a strong dependence on mono-olein concentration at any given frequency; E^* increases from ~ 2 mN/m to ~ 20 mN/m as mono-olien concentration decreases from 1 mg/ml to 0.001 mg/ml. This concentration dependence of E^* is due to the concentration dependence of $\omega_0 \cong D_s/(h_p)^2 = D_s/\left(\frac{\Gamma_{eq}}{c}\right)^2$. As concentration increases, the depletion depth, h_p, decreases and ω_0 increases. Hence, as concentration increases at any given ω, $E^*(\omega)\to 0$. This means that the mono-olein can exchange with the fuel subphase quickly enough that the

interfacial concentration is always in equilibrium, and the interfacial tension remains constant. This leads to smaller values of E^* with concentration, as observed here. However, at lower concentrations, the depletion depth increases and ω_0 decreases, surfactant exchange between the interface and subphase is slowed, the interface does not have time to equilibrate and the interface concentration and interfacial tension change with compression of the interface; hence E^* is larger.

Figure 5B shows the phase angle, ϕ, between the applied strain (area change, $\Delta A/A$) and the resolved stress ($\Delta\gamma/\gamma$). At low concentrations, $\phi \sim 0°$, and increases to $\sim 45°$ with increasing concentration, signifying a gradual change from an elastic to a viscoelastic interface. The elastic, E', ($E' = E^* \cos\phi$) and viscous, E'', ($E'' = E^* \sin\phi$) contributions to the dilatational modulus $|E^*| = \left((E')^2 + (E'')^2\right)^{1/2}$ as a function of mono-olein concentration at selected frequencies are shown in **Figures 5C and D**. At low concentrations over the entire frequency range, $E^* \sim E'$, consistent with the minimal exchange of mono-olein with the subphase as $\omega > \omega_0$. For these films, E' is related to the compressibility of the effectively insoluble film and there is minimal dissipation during expansion and compression. As the concentration increases, the elastic modulus, E', goes through a maximum at 0.005 mg/mL, although E'' is still ~ 5 times smaller than E' at this concentration (note the difference in scales between **Figs. 5 C and D**). The scatter in E'' is much greater than in E' because ϕ is small and the CPM resolution is ~ 1 mN/m.

These trends in the elastic and viscous modulus of mono-olein are similar to those observed by Yang et al.[68] for $C_{12}DMPO$ (dodecyldimethyl phosphine oxide) at the air-water interface using a millimeter-sized sessile drop apparatus. Like mono-olein, $C_{12}DMPO$ is a

soluble, non-ionic surfactant. Moreover, the values of κ and Γ_∞ in the Langmuir model (Eqn. 8) for mono-olein, are similar to that of $C_{10}DMPO$,[69] another surfactant in the same series of nonionic surfactants. Hence, the depletion depth and characteristic frequency, ω_0, for $C_{12}DMPO$ and $C_{10}DMPO$ should also be similar to mono-olein. Qualitatively, the behavior observed in the elastic and viscous modulus for mono-olein is also similar to that reported by Stubenrauch and Miller[70] for $C_{10}E_4$, a nonionic surfactant. This suggests that it is the transport properties of surfactants captured by ω_0 that dictate the dilatational modulus, even though here mono-olein is adsorbed at the fuel-water interface instead of an air-water interface. Zhang et al.[71] used millimeter-sized droplets in an oscillating pendant drop tensiometer, and found that the effective dilatational modulus for mono-olein in clay-treated diesel fuel slightly increased with increasing mono-olein concentration over the range $2.4 - 36.2 \times 10^{-5}$ M over the frequency range of 0.1-0.5 Hz. This work is difficult to compare directly with as those authors used 50% pure mono-olein with no discussion of the contaminants. In general, however, for both sessile[68] and pendant drop[71] analyses that rely on drop shape changes to determine surface tension, the deformation, by definition, can never be at constant shape or purely dilatational. Quantitatively, for millimeter size droplets used in pendant and sessile drop analysis, the Bond number, $\Delta\varrho g R^2 / \gamma \sim 1$, so any deformation process is a complex combination of interfacial dilation and shear and errors can be large. For small values of E^*, it is likely that the shear component may alter the concentration and frequency behavior of the reported dilatational modulus significantly.[48]

Figure 6A shows a frequency sweep of E^* for 0.01X, 0.5X, 0.1X and 0.5X concentrations of PIBSI at the fuel-water interface in the CPM. PIBSI shows a modest increase in the magnitude of the dilatational modulus with frequency, similar to mono-olein at fuel-water interfaces. However, E^* for PIBSI ranges from ~ $40 - 90$ mN/m compared to $1 - 30$ mN/m for mono-olien

(**Figure 5A**). **Figure 6A** also shows that E^* for PIBSI decreases monotonically with increasing surfactant concentration, similar to mono-olein, suggesting that as concentration increases, $\omega_0 \cong$

$$D_s \Big/ (h_p)^2 = D_s(1 + \kappa C_0)^2 \Big/ (\Gamma_\infty \kappa)^2$$ increases. The depletion depth decreases and the

characteristic diffusion frequency ω_0 increases with increasing bulk concentration, making exchange of PIBSI with the subphase more efficient. Hence, $\omega < \omega_0$ over the frequency range examined, which in turn leads to a decrease in E^* with concentration. PIBSI molecules have at least one polyimide head capable of ionizing for each polyisobutylene (PIB) tail; the greater the number of polyimide head groups, the better is the adsorption to the fuel-water interface.[10] In this study, the precise structure of the PIBSI molecules in the additive package is unknown. However, it is possible that interactions between molecules at the interface with water leading to ionization may prevent rapid equilibration of the interface, especially at micrometer length scales where adsorption-desorption kinetics are important.
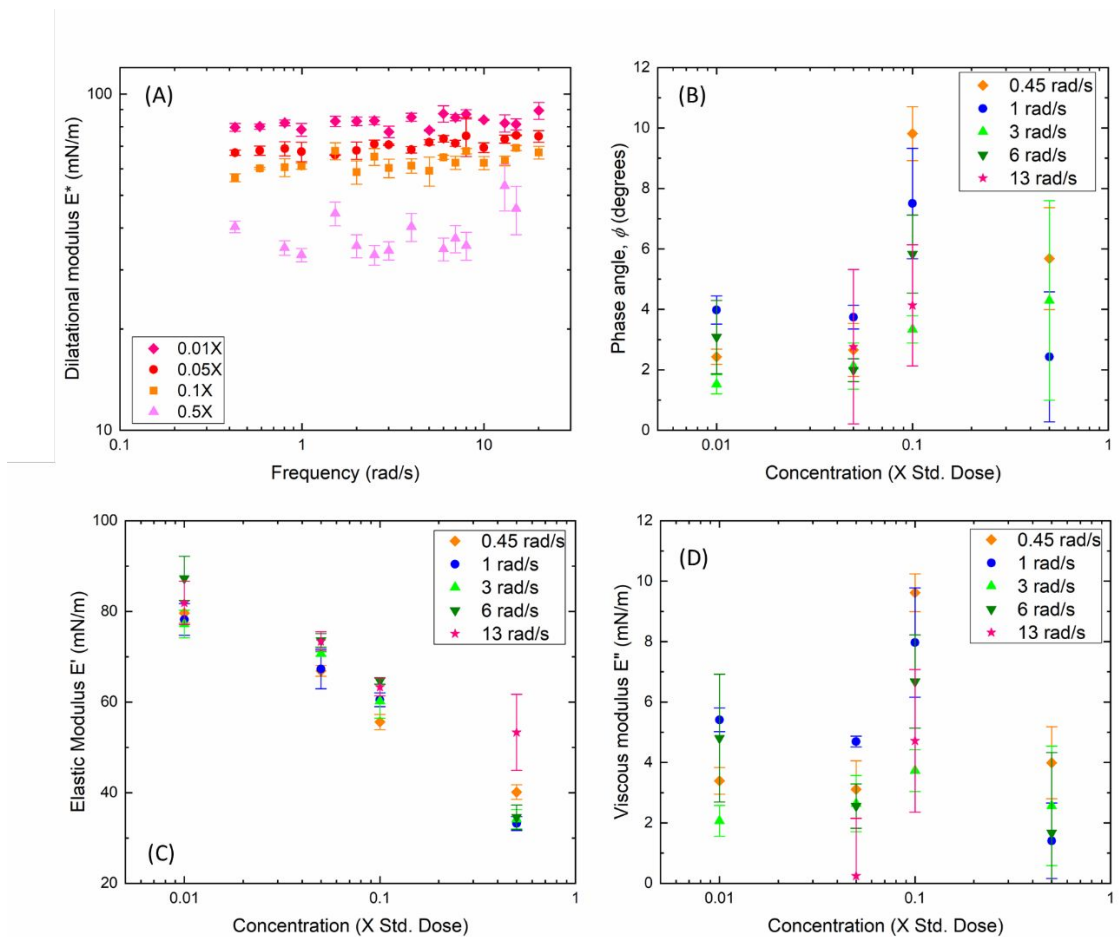
Figure 6 (A) Magnitude of the interfacial dilatational modulus (E*) for PIBSI in CT ULSD as a function of frequency, for four concentrations of PIBSI. (B) Phase angle (ϕ) as a function of PIBSI concentration at selected oscillation frequencies. The phase angle is close to zero at all concentrations, indicating the predominantly elastic nature of the interface. (C) Elastic or storage modulus (E') as a function of PIBSI concentration at selected oscillation frequencies. E* ~ E' over much of the frequency range. (D) Viscous or loss modulus (E") as a function of PIBSI concentration at selected oscillation frequencies.

Figure 6B shows the phase angle, ϕ, between the applied strain (area change, $\Delta A/A$) and the resolved stress ($\Delta \gamma/\gamma$) for PIBSI. Unlike mono-olein, for all PIBSI concentrations and frequencies, $\phi \sim 0°$, signifying an elastic interface with minimal exchange between the interface and subphase fuel. As a result, **Figure 6C, D,** show that, $E^* \sim E'$ and the film is primarily elastic for all concentrations and frequencies. As for mono-olein, the viscous modulus, E'', (**Figure 6D**) exhibits much more uncertainty, likely because E'' is an order of magnitude lower

value than the elastic modulus; small errors in the phase angle, ϕ near zero can lead to large relative changes in $E^{"}$. PIBSI systems have a higher absolute modulus E^* compared to the mono-olein systems, which correlates with the larger depletion depth for PIBSI relative to mono-olein (**Table 2**). We present a more detailed theoretical explanation of the concentration and frequency dependence of dilatational modulus, and the underlying relation to surfactant transport, in the following section.

Dilatational Modulus – Theory

Kotula and Anna[47] added curvature and viscous resistance to drop interface motion corrections to the classical Lucassen and Van Den Tempel model for the dilatational modulus based on diffusion-controlled transport to fluid interfaces.[52,72] They find that the interfacial dilatational modulus (E^*) of a surfactant-laden interface relates the surface-excess stress to the interfacial dilatational strain, and consists of real (elastic) and imaginary (viscous) parts, given by:

$$E^* = E' + iE" = \frac{d\gamma}{dlnA} + i\kappa_s\omega. \quad (18)$$

Here, ω is the frequency of oscillation and κ_s is the dilatational viscosity arising from the dissipative or out-of-phase response to the applied oscillation. Kotula and Anna's analysis[47] assumes that the interface is Newtonian, meaning that the Boussinesq-Scriven constitutive equation[73] can be applied, and the dilatational viscosity κ_s is independent of the oscillation frequency. The dilatational modulus that results is[56]

$$E^* = \frac{\varepsilon_0}{1 + \left(\dfrac{\omega_R}{i\omega}\right)^{\frac{1}{2}}\left(\dfrac{\omega_0}{i\omega}\right)^{\frac{1}{2}} + \left(\dfrac{\omega_0}{i\omega}\right)^{\frac{1}{2}}} + i\kappa_s\omega. \#(19)$$

Here, ε_0 is the limiting or high-frequency modulus. Two characteristic frequencies arise from the analysis, $\omega_R = {D_s}/{R_{eq}^2}$, which accounts for the curvature of a droplet oscillating around an equilibrium radius R_{eq}. The second is ω_0, which accounts for surfactant exchange between the interface and bulk phase as shown in **Figure 2**, $\omega_0 = D_s\left(\frac{dC}{d\Gamma_{eq}}\right)^2 \approx D_s\left(\frac{C}{\Gamma_{eq}}\right)^2$, as described previously. For the experiments in this study, the diffusivity D_s was evaluated independently, from the adsorption kinetics (**Table 2**). R_{eq} is the equilibrium drop radius for a given capillary pressure and interfacial tension prior to initiating the drop oscillation. Hence, for a given experiment, the value of ω_R is fixed, and Eqn. 19 can be fit to the dilatational modulus data with ω_0, κ_s and ε_0 as free parameters to obtain the characteristic frequency for surfactant exchange.
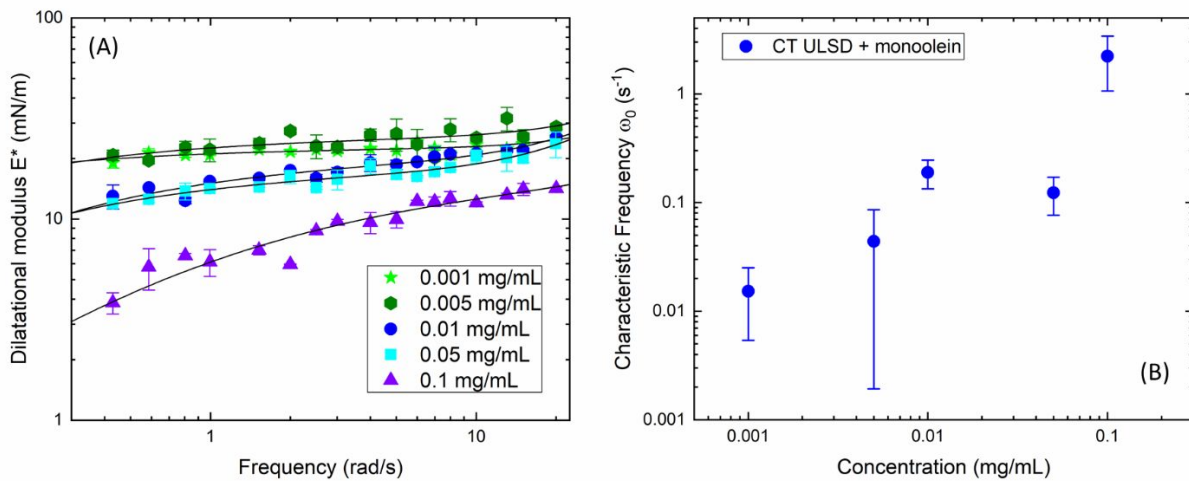
Figure 7 (A) Magnitude of the interfacial dilatational modulus (E*) for mono-olein in CT ULSD as a function of frequency, for various concentrations of mono-olein. The solid black lines indicate fits of Equation (19) to the E* data. (B) Characteristic frequency, ω_0, of surfactant exchange with the subphase obtained from the the fits to the data in (A), as a function of mono-olein concentration. Table 3 shows the comparison between the fit values of ω_0 and those calculated from independently determined equilibrium parameters $\omega_0 \cong \dfrac{D_s(1 + \kappa C_0)^2}{(\Gamma_\infty \kappa)^2}$, Error bars indicate uncertainties in the fit parameter.

The fits of Equation 18 to the dilatational modulus data for water-in-fuel systems containing mono-olein is shown in **Figure 7A,** while the values of the characteristic frequency for diffusion, ω_0, obtained from the fit are plotted as a function of concentration in **Figure 7B**.[56] The value of ω_0 is a key metric for understanding the dynamic response of the surfactant at the interface to deformation, indicating how quickly the surfactant can re-equilibrate the perturbed interface. If the applied frequency of oscillation, $\omega < \omega_0$, diffusion is sufficiently fast that the surfactant at the interface remains in equilibrium with the bulk concentration. Hence, the interfacial concentration, Γ, remains roughly constant and the interfacial tension, γ remains at γ_{eq}, or $\Delta\gamma \sim 0$ as the drop area changes by ΔA. As a result, $E^* = A\left(\dfrac{\partial \gamma}{\partial A}\right) \sim A(\Delta\gamma/\Delta A) \sim 0$. If the applied frequency exceeds ω_0, diffusion cannot keep pace and the surface concentration changes, leading to changes in the interfacial tension, $\Delta\gamma > 0$ (Eqn. 6) and therefore larger values of the dilatational modulus. As seen from **Figure 7B**, ω_0 increases with surfactant concentration. From the Langmuir isotherm, Eqn. 5, $\dfrac{C_0}{\Gamma_{eq}} = \dfrac{(1 + \kappa C_0)}{\kappa \Gamma_\infty}$, which gives $\omega_0 \cong \dfrac{D_s(1 + \kappa C_0)^2}{(\Gamma_\infty \kappa)^2}$. Hence, we can calculate the values of ω_0 from the values of D_s, κ and Γ_∞ determined from the dynamic and equilibrium interfacial tension data in **Table 2** and compare these to the fit values of ω_0 from the dilatational modulus (**Figure 7**). **Table 3** shows

this comparison which agrees within the errors of both sets of data. Clearly, the measured and calculated values follow the same increasing trend with concentration. For mono-olein, **Figure 7B** suggests that at higher surfactant concentrations, the surfactant re-equilibrates rapidly between the bulk and the interface over this frequency range, and higher frequency oscillations are necessary to hinder the re-equilibration and lead to a larger modulus.

Mono-olein concentration (mg/mL)	Measured ω_0 (s^{-1})	Calculated ω_0 (s^{-1})
0.001 (0.0028 mol/m^3)	0.015 ± 0.01	0.008 ± 0.003
0.005 (0.014 mol/m^3)	0.044 ± 0.042	0.012 ± 0.005
0.01 (0.028 mol/m^3)	0.19 ± 0.06	0.019 ± 0.008
0.05 (0.14 mol/m^3)	0.12 ± 0.05	0.13 ± 0.06
0.1(0.28 mol/m^3)	2.23 ± 1.16	0.4 ± 0.2

Table 3 Measured and calculated values of the characteristic frequency for mono-olein systems
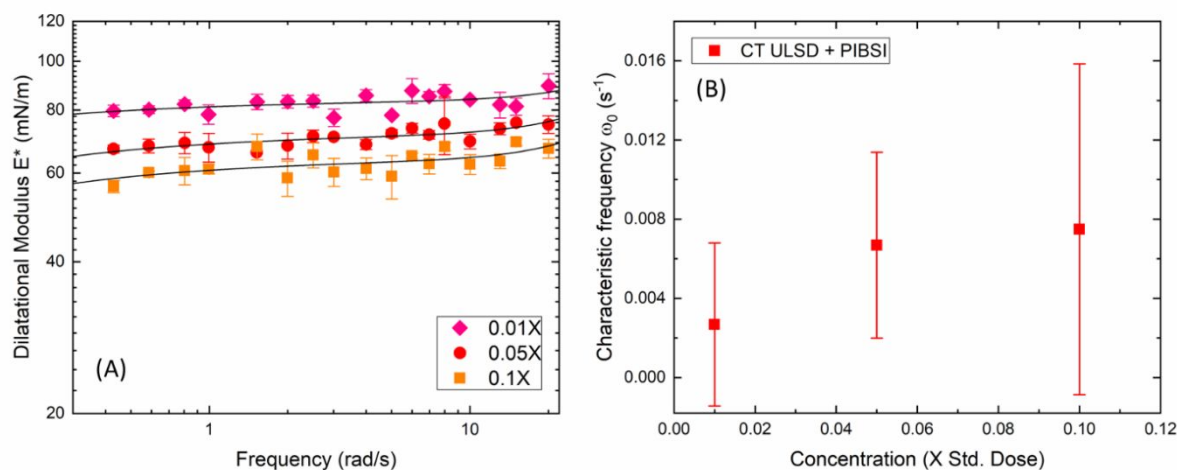
Figure 8 (A) Magnitude of the interfacial dilatational modulus (E*) for PIBSI in CT ULSD as a function of frequency, for various concentrations of PIBSI. The solid black lines indicate fits of Equation (19) to the E* data. (B) Characteristic frequency of surfactant exchange with the subphase obtained from the fits in (A), as a function of PIBSI concentration. Error bars indicate uncertainties obtained from the fits, which are large relative to the values of ω_0, but similar in absolute magnitude to those for mono-olein (Fig. 7B).

Similarly, for PIBSI systems, the fits of Equation (18) to the magnitude of the dilatational modulus E^* at frequencies from 0.01X to 0.1X are shown in **Figure 8A**. We were unable to obtain a good fit to the 0.5X modulus data, likely due to very low interfacial tensions at this PIBSI concentration. The characteristic frequencies ω_0 obtained from the fitting for the three concentrations are shown in **Figure 8B**. Unlike for mono-olein, ω_0 for PIBSI is roughly independent of concentration. From **Tables 1, 2** for the PIBSI concentrations here, $\kappa C_0 \leq 1$, so in this limit, $\omega_0 \cong \dfrac{D_s}{(\Gamma_\infty \kappa)^2}$ and ω_0 should only weakly increase with increasing concentration, unlike mono-olein at higher concentrations where $\kappa C_0 \gg 1$. Moreover, the larger relative errors may be due to the very slow equilibration of water-in-fuel droplets coated with PIBSI; however the absolute errors are of the same magnitude as for mono-olein and likely reflect the inherent limitations of the CPM, such as resolving the radius and pressure drop. The fit and calculated values of $\omega_0 \cong \dfrac{D_s(1 + \kappa C_0)^2}{(\Gamma_\infty \kappa)^2}$ are shown in **Table 4**, both of which indicate that ω_0 depends only weakly on concentration.

PIBSI concentration (X Std. Dose)	Measured ω_0 (s^{-1})	Calculated ω_0 (s^{-1})
0.01 (6.3 x 10^{-4}mol/m^3)	0.0027 ± 0.004	0.0013 ± 0.002
0.05 (3.1 x 10^{-3} mol/m^3)	0.0067 ± 0.005	0.0016 ± 0.002
0.1 (6.3 x 10^{-3} mol/m^3)	0.0075 ± 0.008	0.0022 ± 0.003

Table 4 Measured and calculated values of the characteristic frequency for PIBSI systems

Conclusions:

The measurements presented in this work are important for understanding the interfacial response of droplet interfaces in complex water-in-fuel systems to dilatational or compression-expansion deformation. Over the range of concentrations in this study, typical for water-in-diesel fuel emulsions, the measurements show that over a frequency range of $0.45 - 20$ rad/s, the behavior of the interfacial dilatational modulus of both mono-olein and PIBSI can be explained using the classical theory of Lucassen and Van Den Tempel for diffusion-controlled transport to fluid interfaces[52,72] as modified by Kotula and Anna[47] to account for both the curvature of the interface as well as the viscous resistance to drop interface motion. Fitting this diffusion-limited model to the dilatational data, we find that the characteristic frequency for surfactant exchange with the subphase, $\omega_0 \cong D_s / h_p^2 = D_s(1 + \kappa C_0)^2 / (\Gamma_\infty \kappa)^2$ depends on the depletion depth, h_p, which we modeled using a Langmuir adsorption model: $h_p = \Gamma_{eq} / C_0 = \Gamma_\infty \kappa / 1 + \kappa C_0$. Γ_∞ and κ were independently determined from the equilibrium interfacial tension vs concentration equations of state, $\gamma_0 - \gamma = nR_{ig}T\Gamma_\infty ln(1 + \kappa C_0)$. D_s, the surfactant diffusivity was determined from the dynamic interfacial tension data from pendant drop tensiometry using the Ward and Tordai equation for spherical interfaces. The values of ω_0 from the fit to the Kotula and Anna model matched those calculated from the equilibrium data within experimental error. Thus, we show that interfacial dynamics of water-in-diesel fuel interfaces for surfactant exchange with the subphase can be well explained for these systems by simply using the surfactant properties Γ_∞, κ, and D_s,

It is important to note that in this work, the radius of the droplets was kept relatively constant in the CPM, while the surfactant concentration in diesel fuel was varied. The diffusion-controlled transport-based model developed by Kotula and Anna[47] shows that the dilatational interfacial response is in fact governed by two characteristic frequencies, one of which depends on the radius of curvature of the interface. Previous work by Narayan et al.[4] has shown that as the radius of the water-in-diesel fuel interface is decreased or the curvature increased, the timescale for diffusive exchange becomes shorter. Moreover, Barman et al.[56] showed that increasing the radius of the interface decreases the rate of surfactant exchange with the subphase. Future work will examine the impact of radius of curvature on the dilatational moduli of water-in-diesel fuel interfaces stabilized by mono-olein and PIBSI. It is also known that surfactants at interfaces can form complex morphologies, and that these microstructures at the interface can influence the interfacial rheology. For instance, Sachan and Zasadzinski[74] studied the morphology of lung surfactants at the air-water interface and found that the morphology is associated with the curvature of the interface, which also correlated to a change in the dilatational modulus of the interface. Similarly, Kannan et al.[75] studied the aggregation of monoclonal antibodies at air-aqueous interfaces and found that the antibodies which formed a more cohesive elastic network at the interface gave rise to larger interfacial moduli. However, for the small-molecule soluble surfactants studied in this work, we have not observed any evidence of a microstructure at the interface, particularly at the relatively low surfactant concentrations in this study. The behavior of the interfacial modulus on the microscale at higher surfactant concentrations will be a subject of future work.

Finally, the extent to which dilatational modulus affects droplet coalescence is not yet fully understood, particularly in comparison with other factors such as bulk viscosities, flow

strength and type, droplet size and speed and confinement within filter media. The effect of surface tension gradients caused by drainage of the thin film between coalescing droplets and the resulting Marangoni stress due to the advection of surfactant out of the thin film region is not fully understood either. Real-world diesel fuel is a rather complex mixture consisting of several surface-active species. Whether these water-in-diesel interfaces are stabilized by a viscoelastic surfactant layer at the interface or by Marangoni stress induced by surfactant concentration gradients within the thin film between coalescing droplets remains an open question, which will be explored in future work.

Acknowledgements

References:

1   G. Muschiolik, *Curr. Opin. Colloid Interface Sci.*, 2007, 12, 213–220.

2   C. Washington, *Adv. Drug Deliv. Rev.*, 1996, 20, 131–145.

3   S. Kokal, *SPE Prod. Facil.*, 2005, 20, 5–12.

4   S. Narayan, D. B. Moravec, B. G. Hauser, A. J. Dallas and C. S. Dutcher, *Energy & Fuels*, 2018, **32**, 7326–7337.

5   H. Arouni, U. Farooq, P. Goswami, N. Kapur and S. J. Russell, *SAE Int. J. Fuels Lubr.*, 2018, **11**, 229–238.

6   M. Petiteaux and G. Monsallier, in *SAE Technical Papers*, SAE International, 2009.

7   C. Stanfel, *Filtr. Sep.*, 2009, **46**, 22–25.

8   C. V. Kulkarni, W. Wachter, G. Iglesias-Salto, S. Engelskirchen and S. Ahualli, *Phys. Chem. Chem. Phys.*, 2011, 13, 3004–3021.

9   J. Reid and J. Barker, in *SAE Technical Papers*, SAE International, 2013, vol. 11.

10   S. Pirouz, Y. Wang, J. M. Chong and J. Duhamel, *J. Phys. Chem. B*, 2015, **119**, 12202–12211.

11   H. Naseri, K. Trickett, N. Mitroglou, I. Karathanassis, P. Koukouvinis, M. Gavaises, R. Barbour, D. Diamond, S. E. Rogers, M. Santini and J. Wang, *Sci. Rep.*, 2018, **8**, 1–15.

12   S. Han, Y. Song and T. Ren, *Energy and Fuels*, 2009, **23**, 2576–2580.

13   S. R. Reddy and M. L. McMillan, in *SAE Technical Papers*, 1981, vol. 90, pp. 3598–3616.

14   Society of Automotive Engineers SAE:, *SAE J1488, Revised 1997-08*, .

15   ISO/TC 22/SC 34 Propulsion and powertrain fluids, *ISO 16332:2018*

        Diesel engines — Fuel filters — Method for evaluating fuel/water separation efficiency.

16   W. Stone, G. Bessee and C. Stanfel, *SAE Int. J. Fuels Lubr.*, 2009, **2**, 2009-01–0875.

17   T. C. Chen, J. F. F. Sapitan, F. C. Ballesteros and M. C. Lu, *J. Clean. Prod.*, 2016, **124**, 378–382.

18   Y. Chen, S. Narayan and C. S. Dutcher, *Langmuir*, 2020, acs.langmuir.0c02476.

19   D. Y. C. Chan, E. Klaseboer and R. Manica, *Soft Matter*, 2011, 7, 2235–2264.

20   G. Espinosa and D. Langevin, *Langmuir*, 2009, **25**, 12201–12207.

21   R. Miller, J. K. Ferri, A. Javadi, J. Krägel, N. Mucic and R. Wüstneck, *Colloid Polym. Sci.*, 2010, 288, 937–950.

22   S. Vandebril, A. Franck, G. G. Fuller, P. Moldenaers and J. Vermant, *Rheol. Acta*, 2010, **49**, 131–144.

23   C. F. Brooks, G. G. Fuller, C. W. Frank and C. R. Robertson, *Langmuir*, 1999, **15**, 2450–2459.

24   G. G. Fuller and J. Vermant, *Annu. Rev. Chem. Biomol. Eng.*, 2012, **3**, 519–543.

25   J. Ding, H. E. Warriner, J. A. Zasadzinski and D. K. Schwartz, , DOI:10.1021/la015589.

26   J. Ding, H. E. Warriner and J. A. Zasadzinski, *Phys. Rev. Lett.*, 2002, **88**, 4.

27   S. Q. Choi, K. Kim, C. M. Fellows, K. D. Cao, B. Lin, K. Y. C. Lee, T. M. Squires and J. A. Zasadzinski, *Langmuir*, 2014, **30**, 8829–8838.

28   S. Q. Choi, S. Steltenkamp, J. A. Zasadzinski and T. M. Squires, *Nat. Commun.*, 2011, **2**, 1–6.

29   K. Kim, S. Q. Choi, J. A. Zasadzinski and T. M. Squires, *Soft Matter*, 2018, **14**, 2476–2483.

30   K. Kim, S. Q. Choi, J. A. Zasadzinski and T. M. Squires, *Soft Matter*, 2011, **7**, 7782–7789.

31   K. H. Kim, I. Q. Choi, Z. A. Zell, T. M. Squires and J. A. Zasadzinski, *Proc. Natl. Acad. Sci. U. S. A.*, 2013, **110**, E3054–E3060.

32   Z. A. Zell, A. Nowbahar, V. Mansard, L. G. Leal, S. S. Deshmukh, J. M. Mecca, C. J. Tucker and T. M. Squires, *Proc. Natl. Acad. Sci. U. S. A.*, 2014, **111**, 3677–3682.

33   D. Langevin, *Annu. Rev. Fluid Mech.*, 2014, **46**, 47–65.

34   E. Dickinson, *Colloids Surfaces B Biointerfaces*, 2001, 20, 197–210.

35   S. Narayan, A. E. Metaxas, R. Bachnak, T. Neumiller and C. S. Dutcher, *Curr. Opin. Colloid Interface Sci.*, 2020, 50, 101385.

36   D. Georgieva, V. Schmitt, F. Leal-Calderon and D. Langevin, *Langmuir*, 2009, **25**, 5565–5573.

37   D. Langevin, *Curr. Opin. Colloid Interface Sci.*, 1998, **3**, 600–607.

38   B. A. Noskov, A. V. Akentiev, A. Y. Bilibin, I. M. Zorin and R. Miller, *Adv. Colloid Interface Sci.*, 2003, **104**, 245–271.

39   P. Cicuta, *J. Colloid Interface Sci.*, 2007, **308**, 93–99.

40   D. O. Johnson and K. J. Stebe, *J. Colloid Interface Sci.*, 1994, **168**, 21–31.

41   A. Yeung, T. Dabros and J. Masliyah, *Langmuir*, 1997, **13**, 6597–6606.

42   J. T. Petkov, T. D. Gurkov, B. E. Campbell and R. P. Borwankar, *Langmuir*, 2000, **16**, 3703–3711.

43   N. J. Alvarez, L. M. Walker and S. L. Anna, *Phys. Rev. E - Stat. Nonlinear, Soft Matter Phys.*, 2010, **82**, 11604.

44   N. J. Alvarez, L. M. Walker and S. L. Anna, *Langmuir*, 2010, **26**, 13310–13319.

45   N. J. Alvarez, D. R. Vogus, L. M. Walker and S. L. Anna, *J. Colloid Interface Sci.*, 2012,

372, 183–191.

46   M. D. Reichert, N. J. Alvarez, C. F. Brooks, A. M. Grillet, L. A. Mondy, S. L. Anna and L. M. Walker, *Colloids Surfaces A Physicochem. Eng. Asp.*, 2015, **467**, 135–142.

47   A. P. Kotula and S. L. Anna, *J. Rheol. (N. Y. N. Y).*, 2015, **59**, 85–117.

48   M. Nagel, T. A. Tervoort and J. Vermant, *Adv. Colloid Interface Sci.*, 2017, 247, 33–51.

49   M. D. Reichert and L. M. Walker, *J. Colloid Interface Sci.*, 2015, **449**, 480–487.

50   M. D. Reichert and L. M. Walker, *Langmuir*, 2013, **29**, 1857–1867.

51   J. D. Berry, M. J. Neeson, R. R. Dagastine, D. Y. C. C. Chan and R. F. Tabor, *J. Colloid Interface Sci.*, 2015, **454**, 226–237.

52   J. Lucassen and M. Van Den Tempel, *Chem. Eng. Sci.*, 1972, **27**, 1283–1291.

53   N. J. Alvarez, S. L. Anna, T. Saigal, R. D. Tilton and L. M. Walker, *Langmuir*, 2012, **28**, 8052–8063.

54   N. J. Alvarez, W. Lee, L. M. Walker and S. L. Anna, *J. Colloid Interface Sci.*, 2011, **355**, 231–236.

55   M. L. Davidson and L. M. Walker, *Langmuir*, 2018, **34**, 12906–12913.

56   S. Barman, M. L. Davidson, L. M. Walker, S. L. Anna and J. A. Zasadzinski, *Soft Matter*, , DOI:10.1039/D0SM00415D.

57   G. L. Lin, J. A. Pathak, D. H. Kim, M. Carlson, V. Riguero, Y. J. Kim, J. S. Buff and G. G. Fuller, *Soft Matter*, 2016, **12**, 3293–3302.

58   N. J. Alvarez, Carnegie Mellon University, 2011.

59   F. Jin, R. Balasubramaniam and K. J. Stebe, *J. Adhes.*, 2004, **80**, 773–796.

60   H. Niino and N. Misawa, *J. Atmos. Sci.*, 1984, **41**, 1992–2011.

61   J. Eastoe and J. S. Dalton, *Adv. Colloid Interface Sci.*, 2000, 85, 103–144.

62   H. Manikantan and T. M. Squires, *J. Fluid Mech.*, 2020, 892, 1.

63   S. -Y Lin, K. McKeigue and C. Maldarelli, *AIChE J.*, 1990, **36**, 1785–1795.

64   Y. He, P. Yazhgur, A. Salonen and D. Langevin, *Adv. Colloid Interface Sci.*, 2015, 222, 377–384.

65   A. F. H. Ward and L. Tordai, *J. Chem. Phys.*, 1946, **14**, 453–461.

66   C. A. Miller, *Colloids and Surfaces*, 1988, **29**, 89–102.

67   A. P. Kotula and S. L. Anna, *Soft Matter*, 2016, **12**, 7038–7055.

68   J. Yang, K. Yu, T. Tsuji, R. Jha and Y. Y. Zuo, *J. Colloid Interface Sci.*, 2019, **537**, 547–553.

69   N. Mucic, A. Javadi, N. M. Kovalchuk, E. V. Aksenenko and R. Miller, *Adv. Colloid*

Interface Sci., 2011, 168, 167–178.

70   C. Stubenrauch and R. Miller, *J. Phys. Chem. B*, 2004, **108**, 6412–6421.

71   Q. Zhang, Y. Li, L. Cao, L. Li, K. Huang, W. Li and C. Yang, *Energy and Fuels*, 2019, **33**, 9055–9066.

72   D. Langevin and F. Monroy, *Adv. Colloid Interface Sci.*, 2014, 206, 141–149.

73   L. E. Scriven, *Chem. Eng. Sci.*, 1960, **12**, 98–108.

74   A. K. Sachan and J. A. Zasadzinski, *Proc. Natl. Acad. Sci. U. S. A.*, 2017, **115**, E134–E143.

75   A. Kannan, I. C. Shieh, D. L. Leiske and G. G. Fuller, *Langmuir*, 2018, **34**, 630–638.